

A matched-peak inversion approach for ocean acoustic travel-time tomography

E. K. Skarsoulis

*Institute of Applied and Computational Mathematics, Foundation for Research and Technology Hellas,
P.O. Box 1527, 711 10 Heraklion, Crete, Greece*

(Received 11 May 1999; revised 5 November 1999; accepted 18 November 1999)

A new approach for the inversion of travel-time data is proposed, based on the matching between model arrivals and observed peaks. Using the linearized model relations between sound-speed and arrival-time perturbations about a set of background states, arrival times and associated errors are calculated on a fine grid of model states discretizing the sound-speed parameter space. Each model state can explain (identify) a number of observed peaks in a particular reception lying within the uncertainty intervals of the corresponding predicted arrival times. The model states that explain the maximum number of observed peaks are considered as the more likely parametric descriptions of the reception; these model states can be described in terms of mean values and variances providing a statistical answer (matched-peak solution) to the inversion problem. A basic feature of the matched-peak inversion approach is that each reception can be treated independently, i.e., no constraints are posed from previous-reception identification or inversion results. Accordingly, there is no need for initialization of the inversion procedure and, furthermore, discontinuous travel-time data can be treated. The matched-peak inversion method is demonstrated by application to 9-month-long travel-time data from the Thetis-2 tomography experiment in the western Mediterranean sea. © 2000 Acoustical Society of America. [S0001-4966(00)00203-4]

PACS numbers: 43.30.Pc, 43.30.Bp, 43.60.Lq [DLB]

INTRODUCTION

Ocean acoustic travel-time tomography was introduced by Munk and Wunsch^{1,2} as a remote-sensing technique for monitoring the ocean interior over large sea areas using low-frequency sound waves. Measuring the travel times of pulsed acoustic signals propagating through the water mass over a multitude of different paths, and exploiting the knowledge about how travel times are affected by the sound-speed (temperature) distribution in the water, the latter can be obtained by inversion.

Various modeling approaches have been used for establishing functional relations (model relations) between sound-speed and travel-time variations, based on the notion of ray arrivals,^{3,4} modal arrivals,^{3,5} or peak arrivals.^{6,7} Assuming small perturbations of the ocean, the model relations are usually linearized about a single background state permitting the rapid computation of arrival times directly for any given sound-speed profile. By replacing the single background state through a discrete set of background states, the linearization approach can be extended to cover cases where the initial model relations exhibit significant nonlinearity, either due to the extent of ocean variability (e.g., large variations) or due to the particular propagation conditions.^{8,9}

Before addressing the inversion problem in travel-time tomography, the peak identification problem has to be solved, i.e., the model peaks must be associated with the observed ones.^{10,11} Traditionally this problem is solved by first obtaining observed peak tracks (tracking problem) which are then associated with model peaks (identification problem). Various automatic tracking and identification approaches have been developed based on adaptive filtering,^{12,13} statistical decision theory,^{14,15} or using addi-

tional arrival-angle information.^{16,17} More recently, unified model-based approaches were proposed treating the peak tracking and identification problem in close relation to the inversion problem.^{7,18,19}

A common feature of the automatic tracking and identification algorithms is that identification/inversion results from previous receptions are used to constrain the set of trial identifications in the current reception. Although this approach in general works well in the case of low-noise receptions with stable and well-separated peaks, in cases of noisy data with peaks fading in and out or in case of nonsmooth evolution of arrival times, from reception to reception, tracking may become ambiguous and misidentifications are probable. In such cases, a misidentification in a particular reception may become fatal for the inversions in the subsequent receptions, which may lose track of the correct peaks.¹⁹

A matched-peak inversion approach is proposed here which bypasses the explicit solution of the identification problem and the above inherent difficulties. Using the linearized model relations between sound-speed and arrival-time perturbations, about a set of background states, arrival times and associated model errors are calculated on a fine grid of model states discretizing the parameter space. Each model state can explain (identify) a number of observed peaks in a particular reception lying within the error intervals of the corresponding predicted arrival times. The model states that explain the maximum number of observed peaks are considered as the more likely parametric descriptions of the reception; these model states can be described in terms of mean values and variances providing a statistical answer (matched-peak solution) to the inversion problem. This approach can

be considered as an extension of the matched-field/waveform approach^{20–22} to the case of travel-time data. An advantage of the proposed method is that each reception can be analyzed independently of the previous receptions, i.e., no constraints are posed using results from the previous reception(s). This has an important consequence that there is no need for initialization of the inversions, i.e., no need for additional initialization data, whereas it enables the treatment of discontinuous (gapped) data.

The contents of the work are organized as follows: Sec. I deals with the parametrization of the sound-speed profile, the model relations between the sound-speed parameters and the peak arrival times, as well as with the linearization of the model relations. Section II describes the matched-peak approach starting with the discretization of the parameter space. An association between observed and model peaks is proposed, taking into account the discretization error as well as the observation/model error. In Sec. III the proposed method is applied to 9-month-long tomography data from the Thetis-2 experiment conducted from January to October 1994 in the western Mediterranean sea. Finally, in Sec. IV the main features of the method are discussed and conclusions are drawn.

I. MODEL RELATIONS

A tomographic setting is considered with a broadband source and a receiver at fixed locations in a range-independent ocean. The variability of the sound-speed profile $c(z)$ within the water column can be represented parametrically through a modal expansion of the form

$$c(z) = c_0(z) + \sum_{l=1}^L \vartheta_l \phi_l(z), \quad (1)$$

where $c_0(z)$ is a basic reference profile and $\{\phi_l(z)\}$ is a set of sound-speed modes, e.g., planetary modes or empirical orthogonal functions (EOFs) for the area of interest. The parameter vector $\boldsymbol{\vartheta} = \{\vartheta_l\}$ takes values from the domain Θ spanning the anticipated sound-speed variability.

The solution of the direct problem in ocean acoustic travel-time tomography leads to a set of model relations

$$\tau_i = g_i(\boldsymbol{\vartheta}), \quad i = 1, 2, \dots, I, \quad \boldsymbol{\vartheta} \in \Theta, \quad (2)$$

nonlinear in general, between the parameter vector $\boldsymbol{\vartheta}$ and the arrival times τ_i , $i = 1, 2, \dots, I$. Arrival times may be defined in various ways, using ray theory (ray arrival times),^{1,4} normal-mode theory (modal arrival times),^{3,5} or a unified peak-arrival approach^{6,7} able to cope with either ray- or wave-theoretic modeling approaches. The precise form of Eq. (2) depends on the definition of arrival times and the propagation modeling used. The selection of one or the other definition and approach relies on the ability to resolve the particular model observables in the measured arrival patterns.

For small sound-speed variations, the relations (2) are usually linearized about a mean background state $\boldsymbol{\vartheta} = \boldsymbol{\vartheta}^{(b)}$, $\tau_i^{(b)} = g_i(\boldsymbol{\vartheta}^{(b)})$

$$\tau_i(\boldsymbol{\vartheta}) = \tau_i^{(b)} + \sum_{l=1}^L \frac{\partial g_i(\boldsymbol{\vartheta}^{(b)})}{\partial \vartheta_l} [\vartheta_l - \vartheta_l^{(b)}]. \quad (3)$$

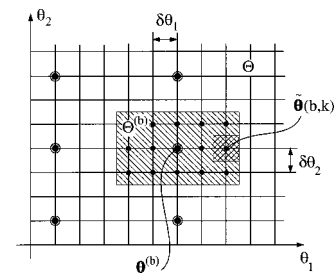


FIG. 1. A schematic diagram of the discretization of the parameter domain for the two-dimensional case.

The derivatives $\partial g_i / \partial \vartheta_l$, called influence coefficients, can be expressed and calculated in terms of background quantities and sound-speed modes.^{4–6} Equation (3) can be used as a basis for linear inversions of travel-time data.

Replacing the single background state with a set of background states, the above linearization approach can also be extended to cover cases where the initial model relations exhibit significant nonlinearity, either due to the extent of ocean variability (e.g., large variations) or due to the particular propagation conditions. The superscript b is considered as a variable index in this case, $b \in \mathcal{B}$, from the background set \mathcal{B} . The set of background states $\boldsymbol{\vartheta}^{(b)}$, $b \in \mathcal{B}$, divides the initial parameter domain Θ into a number of local subdomains $\Theta^{(b)}$, as shown in Fig. 1 (for the two-dimensional case), over which the linearized model relations (3) can be used. In this way, the initial nonlinear model relations (2) are replaced by a set of linear ones.

Ocean acoustic tomography aims at obtaining the range-averaged ocean properties from a single source–receiver pair. In this connection, the model relations (2) and (3) describe the functional dependence of arrival times on variations of the sound-speed profile $c(z)$ for the range-independent case. Nevertheless, the effects of range dependence, which is present either in the medium (e.g., mesoscale eddies) or at the boundaries (e.g., sea-surface roughness), are contained in the received signals and their description/modeling is necessary in order either to correct or to invert for them. Previous studies have shown that the effects of range dependence on the arrival times are primarily of second order.^{23–25} In the following, it is assumed that the main range-dependence effects have been either corrected for (cf. Sec. III A and Ref. 19) or taken into account as part of the observation error.

II. MATCHED-PEAK INVERSION

The matched-peak solution to the inversion problem consists of finding the population of model states that interpret (identify) the maximum number of peaks in each reception. For this purpose the parameter domain is discretized into a finite set of model states. Using the linearized model relations, arrival times are predicted for each model state and compared with the observed ones seeking to maximize the number of matched peaks.

A. Parameter-domain discretization

Besides the grid of background states, a finer grid of model states is introduced with resolution defined by $\delta \theta_l$,

$l=1,\dots,L$, as shown in Fig. 1. The discrete model states within each local parameter domain $\Theta^{(b)}$ are denoted by $\tilde{\boldsymbol{\vartheta}}(b,k)$, where $b \in \mathcal{B}$ is the background index and $k \in \mathcal{K}$ is a local grid index. The linearized model relations can be used within each local parameter grid to calculate the corresponding arrival times

$$\tilde{\tau}_i(b,k) = \tau_i^{(b)} + \sum_{l=1}^L \frac{\partial g_i(\boldsymbol{\vartheta}^{(b)})}{\partial \vartheta_l} [\tilde{\vartheta}_l(b,k) - \vartheta_l^{(b)}]. \quad (4)$$

Due to the finite resolution of the model grid, certain tolerances (discretization errors) have to be accounted for when associating model arrivals and observed peaks. Considering the influence area of each discrete model state to extend half the way to the neighboring model states—cf. Fig. 1, i.e., over the domain described by the Cartesian product $\Pi_{l=1}^L [\tilde{\vartheta}_l(b,k) - \delta\vartheta_l/2, \tilde{\vartheta}_l(b,k) + \delta\vartheta_l/2]$, and exploiting the linearized model relations about the corresponding background state, an estimate for the upper bound of the discretization error can be obtained

$$d_i(b, \delta\boldsymbol{\vartheta}) = \frac{1}{2} \sum_{l=1}^L \left| \frac{\partial g_i(\boldsymbol{\vartheta}^{(b)})}{\partial \vartheta_l} \delta\vartheta_l \right|. \quad (5)$$

The discretization error depends on the particular model peak, the background state, and the discretization step. If a larger step size, i.e., a coarser model grid, is used, the discretization error increases. With decreasing step size (finer model grid), the discretization error decreases accordingly.

Apart from the discretization error, the predicted arrival times are also subject to a modeling error (e.g., due to linearization or range-dependence effects), whereas the arrival-time observation is subject to an error as well. Denoting by n_i the cumulative observation and modeling error, the total tolerance that has to be allowed for when matching predicted arrival times, corresponding to the discrete model states, with observed travel-time data is given by the sum

$$\varepsilon_i(b, \delta\boldsymbol{\vartheta}) = d_i(b, \delta\boldsymbol{\vartheta}) + n_i. \quad (6)$$

B. Peak matching

The observed arrival times τ_j^{obs} , $j=1,\dots,J$ are allowed to associate with the model arrival times $\tilde{\tau}_i(b,k)$, $i=1,\dots,I$ corresponding to the discrete model state $\tilde{\boldsymbol{\vartheta}}(b,k)$, where $b \in \mathcal{B}$, $k \in \mathcal{K}$, if their time difference is smaller than the tolerance ε_i . Accordingly, an association set can be built for each model peak and each discrete model state

$$\mathcal{J}(i;b,k) = \{j \in \{1,\dots,J\} : |\tilde{\tau}_i(b,k) - \tau_j^{\text{obs}}| < \varepsilon_i(b,k)\}, \quad (7)$$

describing the identifiable observed peaks by the particular model peak and model state. Since the search windows may overlap each other, the sets $\mathcal{J}(i;b,k)$ may also partially or totally overlap each other. The number of peaks that a particular model state (b,k) can explain (identify) can be obtained through successive inspection of all association sets by assigning the first available (i.e., not already assigned) observed peak in each association set to the corresponding model peak. This recursive process can be formulated as follows: Assign the first observed peak from $\mathcal{J}(1;b,k)$ to the

first model peak. A zero denotes empty window, i.e., no assignment

$$j_a(1;b,k) = \min(\mathcal{J}(1;b,k) \cup \{0\}). \quad (8)$$

For each subsequent set $\mathcal{J}(i;b,k)$, $i=2,\dots,I$ assign the first available (not already assigned) peak to the corresponding model peak. A zero denotes no assignment, either due to an empty window or due to the assignment of all peaks within the particular window to previous model peaks.

$$j_a(i;b,k) = \min(\{j \in \mathcal{J}(i;b,k) : j > j_a(i-1;b,k)\} \cup \{0\}),$$

$$i=2,\dots,I. \quad (9)$$

The number of identified (assigned) peaks can be calculated by introducing a binary counter $m(i;b,k)$ for each model peak, which is 0 if the peak is not identified in the data and 1 if the peak is identified

$$m(i;b,k) = \begin{cases} 1, & \text{for } j_a(i;b,k) \neq 0, \\ 0, & \text{for } j_a(i;b,k) = 0. \end{cases} \quad (10)$$

The number of peaks identified by the particular model state, called matching index, is given by the sum $M(b,k) = \sum_i m(i;b,k)$. M is an integer number corresponding to each discrete model state and offers a measure of how well the particular observation can be interpreted in terms of identified peaks. The matching index can be calculated very simply and rapidly using the above algorithm. In contrast, automatic identification algorithms have to build up the set of all possible associations between model and observed peaks, which is a computationally intensive procedure since the number of possible combinations may be very large.

In the matched-peak approach, the model states with the largest matching indices, i.e., interpreting the maximum number of observed peaks, are considered the more likely parametric descriptions of the reception

$$\mathcal{Q} = \{(\hat{b}, \hat{k}) \in \mathcal{B} \times \mathcal{K} : M(\hat{b}, \hat{k}) = \max_{b,k} M(b,k)\}. \quad (11)$$

C. A posteriori statistics

The population \mathcal{Q} of the more likely model states can be statistically described in terms of the mean value of the sound-speed parameters

$$\bar{\vartheta}_l = \frac{1}{N} \sum_{(b,k) \in \mathcal{Q}} \tilde{\vartheta}_l(b,k), \quad (12)$$

and the corresponding covariance matrix

$$D_{\vartheta\vartheta,l\lambda} = \frac{1}{N} \sum_{(b,k) \in \mathcal{Q}} (\tilde{\vartheta}_l(b,k) - \bar{\vartheta}_l)(\tilde{\vartheta}_\lambda(b,k) - \bar{\vartheta}_\lambda), \quad (13)$$

where N is the cardinality of the set \mathcal{Q} , i.e., the number of selected model states. Using the parametric expression (1) for the sound speed, the mean sound-speed profile $\bar{c}(z)$ can be calculated from the mean parameter vector $\bar{\boldsymbol{\vartheta}}$. Further, the sound-speed variance $\langle \delta c^2(z) \rangle = \langle [c(z) - \bar{c}(z)]^2 \rangle$ can be expressed as

$$\langle \delta c^2(z) \rangle = \text{diag}[\boldsymbol{\phi}'(z) \mathbf{D}_{\vartheta\vartheta} \boldsymbol{\phi}(z)], \quad (14)$$

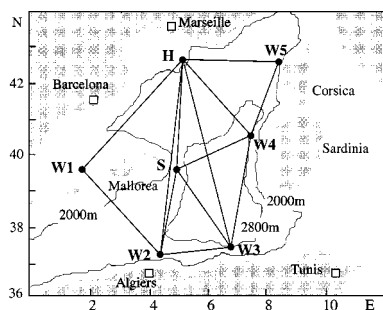


FIG. 2. The geometry of the Thetis-2 experiment in the western Mediterranean.

where $\phi(z) = \{\phi_i(z)\}$ is the vector (column matrix) containing the values of the sound-speed modes at depth z , and $\mathbf{D}_{\theta\theta}$ is the covariance matrix calculated in (13). The variance for the depth-averaged sound speed (over a particular depth layer) is given by $\langle \delta \bar{c}^2 \rangle = \bar{\phi}' \mathbf{D}_{\theta\theta} \bar{\phi}$, where the overbars denote depth-averaged quantities.

III. APPLICATION TO THETIS-2 DATA

The matched-peak inversion method is applied in the following to the Thetis-2 experiment conducted from January to October 1994 in the western Mediterranean sea.^{26,27} Figure 2 shows the experimental site and geometry. The tomographic array contained seven moored transceivers all deployed at a nominal depth of 150 m. A low-frequency (HLF-5) acoustic source, marked by H in Fig. 2, of central frequency 250 Hz and effective bandwidth 62.5 Hz, insonified the basin at 8-h intervals. The remaining six sources ($W1-W5$ and S), transmitting six times per day, were of Webb type with central frequency 400 Hz and effective bandwidth 100 Hz. The receiver parts of $W1-W5$ were modified to listen to both the 400-Hz and 250-Hz signals. Along the section $W3-H$ an expendable bathythermograph (XBT) verification line was occupied every 2 weeks using a commercial vessel connecting Marseilles (France) to Skikda (Algeria). In particular, the positions of H and $W3$ were aligned with the ship's route to allow detailed comparisons between tomographic inversions and XBT data. Tomography data from this particular transect (receptions at $W3$ from H) spanning the period from 24 January to 16 October 1994 (yeardays 24.4–289.4) are analyzed in the following.

A. The data

Figure 3(a) shows the sequence of acoustic receptions at $W3$ from H over the 9-month duration of the experiment, after correlation (matched-filter) processing, clock-drift correction, mooring-motion correction, and offset calibration.^{19,26} A 3-day sliding average has been applied, i.e., for each calendar day the arrival patterns measured from the preceding to the following day have been incoherently averaged. Finally, the arrival patterns in Fig. 3(a) are normalized with respect to the noise rms level. The parts of each reception lying higher than 2.5 times the rms noise level are considered as containing useful signal and they are used for the calculation of the signal-to-noise ratio (SNR) shown in Fig. 3(b). It is seen from both Fig. 3(a) and (b) that there are

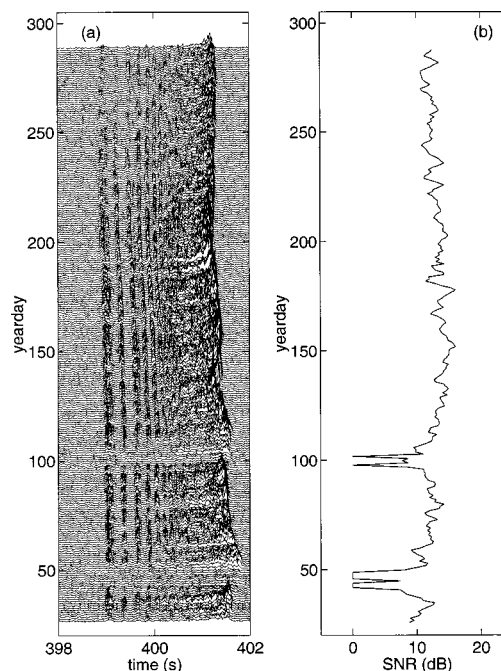


FIG. 3. The acoustic receptions at $W3$ from H . (a) The arrival patterns (3-day incoherent averages) after clock-drift, mooring-motion correction, and offset calibration. (b) The signal-to-noise ratio of the receptions.

two periods, from yearday 37 to 51 and from 96 to 105, characterized by particularly low SNR; over these two periods the transmissions are practically interrupted. A threshold to separate meaningful and poor receptions is 10 dB.

In the first half of most receptions five to six arrival groups can be distinguished which can be associated with particular ray groups corresponding to steep propagation angles. The remaining intermediate and late arrivals are difficult to interpret in terms of ray arrivals because ray groups overlap each other in this interval. To exploit the maximum of information contained in the intermediate and late part of the arrival patterns, the peak-arrival approach^{6,7} is used for describing the observables, combined with normal-mode propagation modeling.

Figure 4 shows the observed peak arrival times corresponding to the receptions of Fig. 3(a). The horizontal axis of this figure represents yeardays of 1994 and spans the pe-

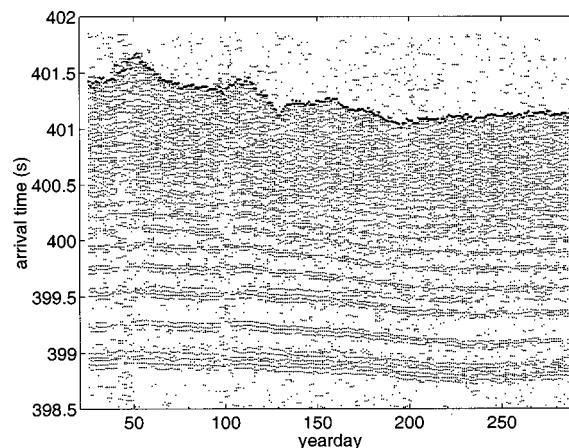


FIG. 4. Measured acoustic arrival times at $W3$ from H . The cutoff peaks are denoted by heavier dots.

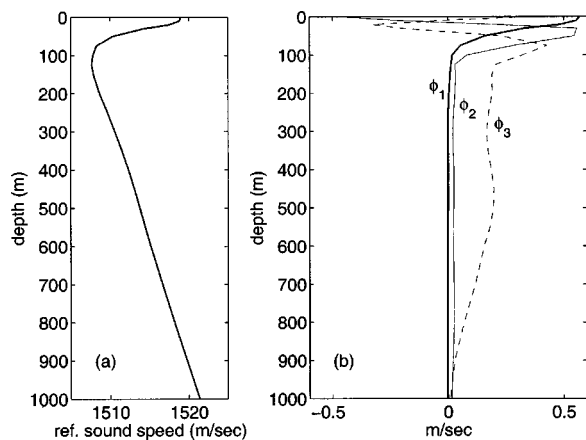


FIG. 5. (a) The basic reference sound-speed profile, and (b) the three most significant empirical orthogonal functions (EOFs) for the western Mediterranean basin.

riod of the experiment, whereas the vertical axis measures arrival time. The 55–60 more-significant peaks in each reception are shown through dots. The location of the cutoff peaks, defined as the last of the five highest peaks in each reception, is shown through heavier dots.

In Fig. 5 the first three empirical orthogonal functions (EOFs) for the western Mediterranean basin are shown along with the basic reference profile. The rms values of the EOF amplitudes are $\vartheta_{1,\text{rms}} = 18.48$, $\vartheta_{2,\text{rms}} = 2.88$, and $\vartheta_{3,\text{rms}} = 0.96$. EOF-1 accounts for the bulk of the seasonal variability taking place close to the surface, and this explains the large rms value of the corresponding amplitude, whereas higher-order EOFs extend to increasingly deep layers. The first three EOFs explain 99.6% of the total variance.

Figure 6(a) shows variations of the reference profile (upper 300 m) in the direction of the first EOF over the ϑ_1 interval $[-50, 50]$, covering 2.5 standard deviations of the corresponding amplitude and spanning the gross seasonal variability expected. Large negative values for ϑ_1 correspond to winter conditions (upward-refracting profile) and large positive values to summer conditions (channeled profiles).

Figure 6(b) shows the predicted peak-arrival times cor-

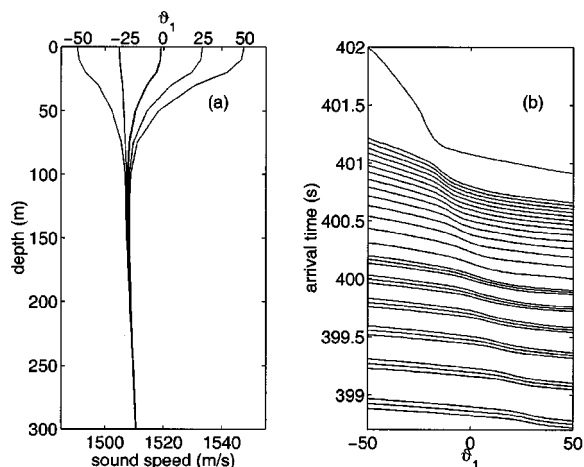


FIG. 6. (a) The sound-speed profiles corresponding to $\vartheta_1 = -50, -25, 0, 25, 50$. (b) The predicted peak arrival times as functions of ϑ_1 .

responding to the different ϑ_1 values for 33 model peaks, from the early arrivals to the final cutoff peak, which could be traced throughout the range of variability. A clear nonlinear behavior can be seen, caused by the passage from surface-reflected propagation in winter to refracted propagation in summer. This passage takes place at different ϑ_1 values for the different peaks, corresponding to sound-speed values at the surface equal to the values at the different turning depths. For an efficient description of the nonlinearity, a fine discretization of the ϑ_1 axis is required.

The set of background states is defined in the following as EOF-1 variations of the basic reference profile over the ϑ_1 interval $[-50, 50]$, covering 2.5 standard deviations of the corresponding amplitude, with a step equal to 2. The influence coefficients $\partial g_i / \partial \vartheta_1$ are calculated for the 33 peak arrivals of Fig. 6(b) at each background state using a KRAKEN²⁸-based normal-mode code.

A time-variable parameter domain (search interval) is considered for ϑ_1 , ± 10 about the historical mean value of ϑ_1 for each day of the year; the anticipated maximum standard deviation from historical data²⁹ is 1.9. The restriction of the parameter domain for ϑ_1 significantly reduces the computational burden by avoiding calculations for unnatural model states which lie outside the anticipated variability range for each season. For the remaining two EOFs the parameter domains are taken to cover ± 2.5 standard deviations of the corresponding amplitudes, i.e., the interval $[-7.5, 7.5]$ for ϑ_2 and $[-2.5, 2.5]$ for ϑ_3 . The discretization steps are set to $\delta\vartheta_1 = 2/3$, $\delta\vartheta_2 = 0.75$, and $\delta\vartheta_3 = 0.25$.

An observation error of 10 ms is used for all peaks except for the cutoff peak, which is subject to a significant range-dependence effect caused by the large-scale warming trend from north to south. It was shown in a previous study¹⁹ that this causes a cold bias (time delay) to the cutoff peak depending on the background state—the effect is weaker in winter than in summer. In accordance with that study a variable-time correction, linearly varying from 70 ms at $\vartheta_1 = -50$ to 150 ms at $\vartheta_1 = 50$, is applied to the cutoff peak to account for range dependence; after the correction, the observation/model error is set to 50 ms for that peak.

B. Inversion results

Figure 7 shows the distribution of discrete model states identifying the maximum number of peaks in each daily reception. The population density is denoted by the gray scale increasing from white (zero density) to black (maximum density). The gross seasonal trend is seen in the evolution of the first EOF amplitude. The other two EOFs exhibit no major seasonal behavior except for the second one in summer. Also, their probability masses lie away from the boundaries of the search intervals, confirming the proper definition of these intervals. In Fig. 8 the mean values and standard deviations (error intervals) of these distributions are shown. The time-variable search interval for ϑ_1 is also shown in this figure. These estimates for the parameter vector have been obtained from the observed travel-time data without having provided any explicit solution to the identification problem.

The number of peaks matched in each reception is shown in Fig. 9. On the average, 28–30 peaks out of the 33

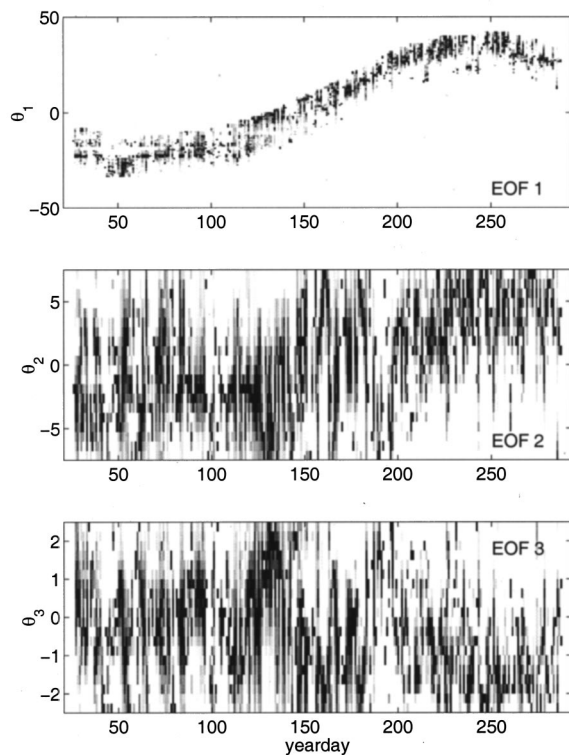


FIG. 7. The distributions of the EOF amplitudes corresponding to the discrete model states identifying the maximum number of peaks in each reception.

model peaks can be identified. In a few receptions the scheme could match as much as 33 peaks, i.e., associate all model peaks with observed ones. During the two periods of low SNR receptions, a lower number of peaks is matched; the drop in the matching index is a warning for possible irrelevance of the selected peaks.

The *a posteriori* distribution of the predicted peak arrival times corresponding to the population of the selected model states for each reception is shown in Fig. 10. The tracks of the 33 model arrivals are recognized in this figure. Nevertheless, these are predicted arrival times corresponding to the more likely model states for each reception and not the identified peaks of each reception. The two periods of low SNR receptions are recognized through systematic discontinuities in the tracks of Fig. 10 pointing to the irrelevance of the selected peaks.

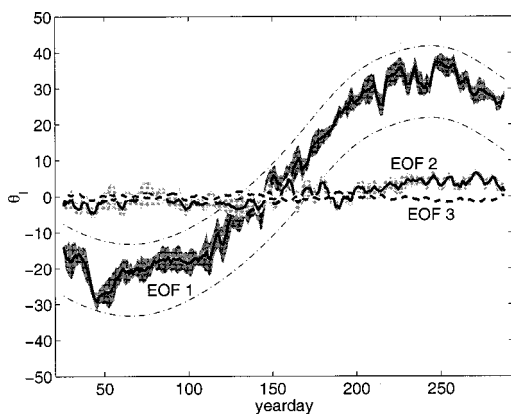


FIG. 8. The mean values and standard deviations (error intervals) of the EOF amplitudes corresponding to the populations of Fig. 7. The dash-dotted lines describe the time-variable parameter domain for ϑ_1 .

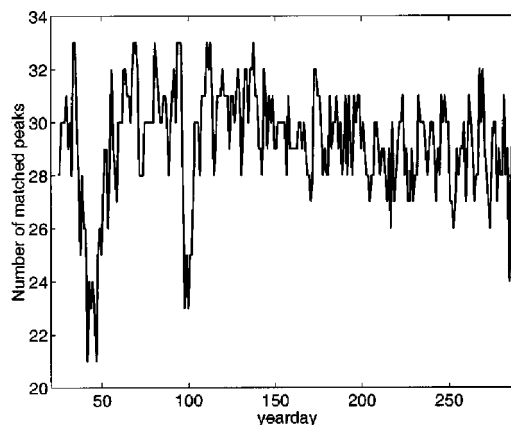


FIG. 9. The number of peaks matched in each reception.

Figure 11 shows the distributions of the depth-averaged temperatures over three layers: a surface layer from the surface down to 150 m, an intermediate layer from 150 to 600 m, and a deep layer from the surface down to 2000 m, representing the total heat content of the water column. A depth-dependent conversion relation, based on historical temperature and salinity data, has been used for obtaining temperature profiles from sound-speed profiles.¹⁹ The gray scale in Fig. 11 represents the population densities of the temperatures corresponding to the more likely model states for each reception. XBT data and also data from conductivity-temperature-density (CTD) measurements during the deployment/recovery cruises are shown in Fig. 11 as crossed circles and squares, respectively. Finally, the dashed lines represent the historical mean temperatures for each day of the year.

From Fig. 11 it is seen that the gross seasonal changes are limited in the surface layer. The observed variability in the intermediate layer, below 150 m, is mainly due to mesoscale activity. The surface layer also determines the evolution of the heat content over the entire water column, represented by the 0–2000-m layer, as shown in the lower panel of Fig. 11. The populations of model states selected using the matching principle give a satisfactory description of the actual evolution described by the XBT data in all three layers.

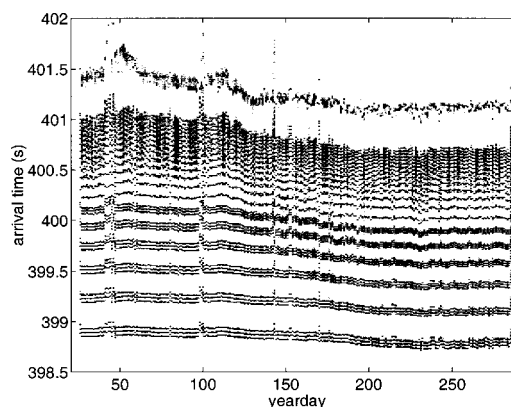


FIG. 10. The distribution of the predicted peak arrival times corresponding to the population of the selected model states for each reception.

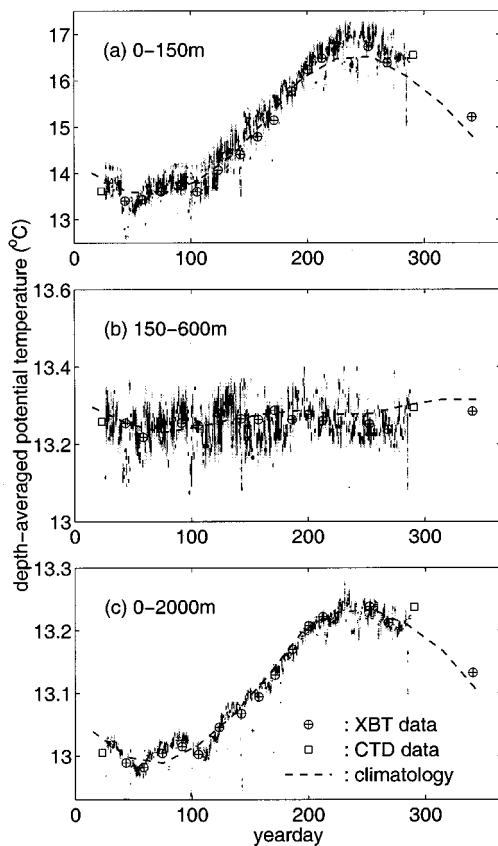


FIG. 11. The distribution of depth-averaged potential temperatures in the 0–150, 150–600, and 0–2000-m layers, corresponding to the discrete model states identifying the maximum number of peaks in each reception, compared with CTD data from the deployment/recovery cruises, with independent XBT data, and also with mean temperatures from the climatology.

The increased spread of the populations in the intermediate and shallow layers, compared to the deep layer, is due to the larger ambiguity in the identification of the intermediate and late arrivals (cf. Fig. 4), associated with these two layers, compared to the well-separated early arrival groups associated with the deep layer.

A clearer picture of the recovered depth-averaged temperatures over the three layers is shown in Fig. 12 in terms of mean values and standard deviations (error intervals) of the distributions of Fig. 11. The results have been smoothed using a five-reception sliding average, whereas the results corresponding to receptions with SNR lower than 10 dB have been ignored. It is seen that the recovered mean temperatures give a satisfactory description of the actual conditions, the XBT data lying in most cases within the estimated error limits. A comparison of the inversions with the climatological data shows that there are deviations from the climatological mean conditions in all three layers and this is also confirmed by the XBT data. The amplitude of the seasonal signal in the surface layer is 10%–20% larger in the observations than in the historical data.

Figure 13 shows a comparison of the XBT temperature profiles in the upper 300 m with the corresponding inversion results (averaged over the time window of each XBT sample) and associated standard deviations (error bars). A fair agreement between the inversion results and the XBT profiles is seen, the observed deviations lying within the in-

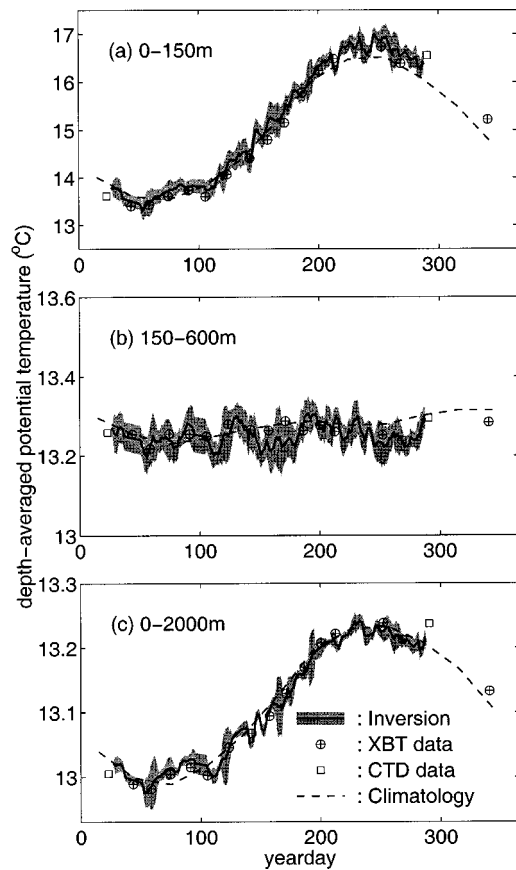


FIG. 12. The mean values and standard deviations (error intervals) of the potential temperatures in the 0–150, 150–600, and 0–2000-m layers, corresponding to the populations of Fig. 11, compared with CTD data from the deployment/recovery cruises, with independent XBT data, and also with mean temperatures from the climatology.

version error bars in most cases. The inversion results underlying the left-most profile fall within the first low-SNR period. The seasonal temperature variability spans about 12 °C at the surface and nearly disappears below 150-m depth. It is also seen that deviations between XBT data and inversions are in general larger in the surface layer than in the deeper layers, and this is consistent with the inversion errors shown. The physical reason for the reduced tomography sensitivity near the sea surface lies in the particular temperature and

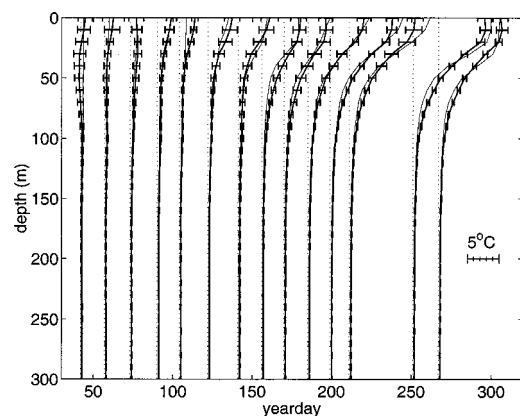


FIG. 13. Comparison of the XBT temperature profiles (deviations from 13.03 °C—light lines) with the corresponding inversion results (heavy lines) and inversion errors.

sound-speed conditions in the Mediterranean, which give rise to either surface-reflected propagation in winter or channelled propagation with a shallow axis in summer. In both cases a very small fraction of the propagation time is spent in the near-surface layer, resulting in a poorer acoustic sampling of smaller depths.

IV. DISCUSSION AND CONCLUSIONS

An inversion approach for travel-time data was proposed which bypasses the explicit solution of the identification problem. This approach uses the linearized model relations between sound-speed and arrival-time perturbations about a set of background states, to calculate arrival times and associated model errors on a fine grid of model states discretizing the sound-speed parameter space. The corresponding model peaks (arrivals) are allowed to associate with observed peaks if their time distance is smaller than a tolerance which depends on the particular peak, the background state, and the discretization step. Accordingly, each discrete model state can explain (identify) a number of peaks in a particular reception. The model states that explain the maximum number of observed peaks are considered the more likely parametric descriptions of the particular reception. Their population forms the matched-peak solution of the inversion problem.

The matched-peak method can be considered an extension of the matched-field approach to the case of travel-time data. The use of the linearized model relations between sound-speed and arrival-time variations accelerates the calculations significantly.

Since the method is based on the number of peaks identified by each model state rather than on inversions for all possible peak identifications in each reception (as is the case in the approaches simultaneously addressing the inversion and identification problem), there is no need to set up the identification space, i.e., the set of all trial identification functions for each reception. The calculation of the number of peaks identified by each model state is a much easier computational task than the setup of the identification space.

A significant advantage of the matched-peak approach is that each reception can be analyzed independently of the previous receptions, i.e., no constraints are posed using identification or inversion results from the previous reception(s). This has an important consequence that there is no need for initialization of the inversion procedure, i.e., no need for additional initialization (commonly hydrographic) data, and also that acoustic data with gaps can be treated. Even though previous-reception results are commonly used in existing methods to assure a smooth evolution of the peak tracks and the inversion results, this strategy may cause errors in a number of cases (e.g., complicated track geometry, peaks fading in and out, discontinuities in the data, or low SNR receptions). In this connection the independent treatment of each reception may result in a nonsmooth evolution of the inversion results, but at the same time it adds to the robustness of the analysis.

The matched-peak inversion approach was initially devised as a simple means to obtain first inversion results from tomography travel-time data, offering an automatic alternative to the usual tracking–identification–inversion approach

and also avoiding the difficulties and possible uncertainties associated with the simultaneous solution of the identification and inversion problem (automatic identification/inversion scheme). Despite its simplicity, the application to 9-month-long travel-time data from the Thetis-2 experiment provided very satisfactory results. The inversion results from a particular section ($W3-H$) were presented here for which systematic XBT observations exist, permitting detailed comparisons.

The robustness of the matched-peak approach has proven particularly valuable in cases of problematic evolution of arrival patterns, either due to nonsmooth evolution of arrival times or due to missing receptions. Such cases were encountered in $W3-H$ and the other Thetis-2 sections, and quite a few of them could not be handled at all by the automatic identification/inversion scheme. With the matched-peak approach all sections—13 in total—have been automatically processed; the systematic results will be published elsewhere.

The matched-peak inversion approach provides no explicit solution for the identification problem. If the solution of this problem is of interest, the matched-peak approach can still provide a means to build up the identification space—the set of all possible identification (association) functions—in a model-based fashion, independently of previous-step constraints.

ACKNOWLEDGMENTS

This work was partially supported by the European Union MAST-III program under Contract No. MAS3-CT97-0147. Fruitful discussions with U. Send (IfM, Kiel) F. Gailard (IFREMER, Brest), and D. Mauuary (LIS, Grenoble) as well as comments by the anonymous reviewers are acknowledged.

- ¹W. H. Munk and C. Wunsch, "Ocean acoustic tomography: A scheme for large scale monitoring," *Deep-Sea Res.* **26A**, 123–161 (1979).
- ²W. H. Munk, P. F. Worcester, and C. Wunsch, *Ocean Acoustic Tomography* (Cambridge University Press, New York, 1995).
- ³W. H. Munk and C. Wunsch, "Ocean acoustic tomography: Rays and modes," *Rev. Geophys. Space Phys.* **21**, 777–793 (1983).
- ⁴J. L. Spiesberger and P. F. Worcester, "Perturbations in travel time and ray geometry due to mesoscale disturbances: A comparison of exact and approximate calculations," *J. Acoust. Soc. Am.* **74**, 219–225 (1983).
- ⁵E. C. Shang, "Ocean acoustic tomography based on adiabatic mode theory," *J. Acoust. Soc. Am.* **85**, 1531–1537 (1989).
- ⁶G. A. Athanassoulis and E. K. Skarsoulis, "Arrival-time perturbations of broadband tomographic signals due to sound-speed disturbances. A wave-theoretic approach," *J. Acoust. Soc. Am.* **97**, 3575–3588 (1995).
- ⁷E. K. Skarsoulis, G. A. Athanassoulis, and U. Send, "Ocean acoustic tomography based on peak arrivals," *J. Acoust. Soc. Am.* **100**, 797–813 (1996).
- ⁸E. K. Skarsoulis, "An adaptive scheme for ocean acoustic tomography of large sound-speed variations," in *Proceedings of the 3rd European Conference on Underwater Acoust.*, edited by J. S. Papadakis (Crete University Press, Heraklion, 1996), pp. 803–808.
- ⁹B. D. Dushaw, P. F. Worcester, B. D. Cornuelle, and B. M. Howe, "Variability of heat content in the central north Pacific in summer 1987 determined from long-range acoustic transmissions," *J. Phys. Oceanogr.* **23**, 2650–2666 (1993).
- ¹⁰J. L. Spiesberger, R. C. Spindel, and K. Metzger, "Stability and identification of ocean acoustic multipaths," *J. Acoust. Soc. Am.* **67**, 2011–2017 (1980).
- ¹¹G. R. Legters, N. L. Weinberg, and J. G. Clark, "Long-range Atlantic

- acoustic multi-path identification," J. Acoust. Soc. Am. **73**, 1571–1580 (1983).
- ¹²R. Hippenstiel, E. Chaulk, and J. H. Miller, "An adaptive tracker for partially resolved acoustic arrivals with application to ocean acoustic tomography," J. Acoust. Soc. Am. **92**, 1759–1762 (1992).
 - ¹³J. H. Miller, J. F. Lynch, C. S. Chiu, E. L. Westreich, J. S. Westreich, R. Hippenstiel, and E. Chaulk, "Acoustic measurements of surface gravity wave spectra in Monterey Bay using mode travel-time fluctuations," J. Acoust. Soc. Am. **94**, 954–974 (1993).
 - ¹⁴F. R. Martin-Lauzer and D. Mauuary, "Probabilistic ray identification: A new tool for ocean acoustic tomography," in Proceedings ICASSP 94 (Adelaide, 1994).
 - ¹⁵D. Mauuary, "Detection, estimation et identification pour la tomographie coustique oceanique. Etude theorique et experimentale," Ph.D. thesis, Institut National Polytechnique de Grenoble, 1994.
 - ¹⁶B. M. Howe, P. F. Worcester, and R. C. Spindel, "Ocean acoustic tomography: Mesoscale velocity," J. Geophys. Res. **92**, 3785–3805 (1987).
 - ¹⁷P. F. Worcester, "An example of ocean acoustic multipath identification at long range using both travel time and arrival angle," J. Acoust. Soc. Am. **70**, 1743–1747 (1981).
 - ¹⁸U. Send, "Peak tracking by simultaneous inversion: Toward a one-step acoustic tomography analysis," J. Atmos. Ocean. Technol. **13**, 1116–1122 (1996).
 - ¹⁹E. K. Skarsoulis and U. Send, "One-step analysis of nonlinear traveltime data in ocean acoustic tomography," J. Atmos. Ocean. Technol. (in press).
 - ²⁰A. Tolstoy, *Matched Field Processing for Underwater Acoustics* (World Scientific, Singapore, 1993).
 - ²¹J.-P. Hermand and W. I. Roderick, "Acoustic model-based matched-filter processing for fading time-dispersive ocean channels: Theory and experiment," IEEE J. Ocean Eng. **OE-18**, 447–465 (1993).
 - ²²J.-P. Hermand, "Broad-band geoacoustic inversion in shallow water from waveguide impulse response measurements on a single hydrophone: Theory and experimental results," IEEE J. Ocean Eng. **OE-24**, 41–66 (1999).
 - ²³J. L. Spiesberger, "Ocean acoustic tomography: Travel time biases," J. Acoust. Soc. Am. **77**, 83–100 (1985).
 - ²⁴W. H. Munk and C. Wunsch, "Biases and caustics in long-range acoustic tomography," Deep-Sea Res. **32**, 1317–1346 (1985).
 - ²⁵J. F. Lynch, J. H. Miller, and C. S. Chiu, "Phase and travel-time variability of adiabatic acoustic normal modes due to scattering from a rough sea surface, with applications to propagation in shallow-water and high-latitude regions," J. Acoust. Soc. Am. **85**, 83–89 (1989).
 - ²⁶Thetis-2, A pilot tomography system for monitoring the western Mediterranean basin, Final Report, edited by U. Send, EU MAST-2 project CT91-0006, March 1996.
 - ²⁷U. Send, G. Krahmann, D. Mauuary, Y. Desaubies, F. Gaillard, T. Terre, J. Papadakis, M. Taroudakis, E. Skarsoulis, and C. Millot, "Acoustic observations of heat content across the Mediterranean Sea," Nature (London) **385**, 615–617 (1997).
 - ²⁸M. B. Porter and E. L. Reiss, "A numerical method for ocean acoustic normal modes," J. Acoust. Soc. Am. **76**, 244–252 (1984).
 - ²⁹P. Brasseur, "The MED2 hydrographic data base (<http://modb.oce.ulg.ac.be>)," Oceanogr. Lit. Rev. **42**, 414–415 (1995).